Development of an Aeroelastic Modeling Capability for Transient Nozzle Side Load Analysis

Ten-See Wang[*]
NASA Marshall Space Flight Center, Huntsville, Alabama, 35812

Xiang Zhao[†],
Alabama A&M University, Huntsville, Alabama, 35762

Sijun Zhang[‡]
ESI CFD, Inc., Huntsville, Alabama, 35806

and
Yen-Sen Chen[§]
Applied Research Laboratory, Hsinchu 30078, Taiwan

Lateral nozzle forces are known to cause severe structural damage to any new rocket engine in development during test. While three-dimensional, transient, turbulent, chemically reacting computational fluid dynamics methodology has been demonstrated to capture major side load physics with rigid nozzles, hot-fire tests often show nozzle structure deformation during major side load events, leading to structural damages if structural strengthening measures were not taken. The modeling picture is incomplete without the capability to address the two-way responses between the structure and fluid. The objective of this study is to develop a coupled aeroelastic modeling capability by implementing the necessary structural dynamics component into an anchored computational fluid dynamics methodology. The computational fluid dynamics component is based on an unstructured-grid, pressure-based computational fluid dynamics formulation, while the computational structural dynamics component is developed in the framework of modal analysis. Transient aeroelastic nozzle startup analyses of the Block I Space Shuttle Main Engine at sea level were performed. The computed results from the aeroelastic nozzle modeling are presented.

[*] Technical Assistant, ER42, Fluid Dynamics Branch, Propulsion Structure, Thermal, and Fluids Analysis Division, Senior Member AIAA.
[†] Associate Professor, Member AIAA.
[‡] Senior Development Engineer, Member AIAA.
[§] Senior Research Fellow, Senior Member AIAA.

Nomenclature

C_1,C_2,C_3,C_μ= turbulence modeling constants, 1.15, 1.9, 0.25, and 0.09.

C = damping

C_p = heat capacity

D = diffusivity

F_{yz}, F_y, F_z = integrated force, and component forces in the lateral direction

f = frequency

H = total enthalpy

K = thermal conductivity or stiffness

k = turbulent kinetic energy

M = mass

Q = heat flux

r = Eigen function

T = temperature

t = time, s

u = mean velocities

V^2 = $\sum u^2$

x = Cartesian coordinates or nondimensional distance

Y = physical displacement

Z = generalized displacement

α = species mass fraction

ε = turbulent kinetic energy dissipation rate

μ = viscosity

μ_t = turbulent eddy viscosity ($=\rho C_\mu k^2/\varepsilon$)

ξ = damping parameter

Π = turbulent kinetic energy production

ρ = density

σ = turbulence modeling constants, 0.9, 0.9, 0.89, and 1.15 for Eqs. (2), (4-6).

τ = shear stress

Φ = mode shape matrix

ω = chemical species production rate or natural frequency

Subscripts

r = radiation

g = mesh movement

t = turbulent flow

I. Introduction

Nozzle lateral forces during engine startup and shutdown transients, if not properly managed, are known to cause severe structural damage to the engine hardware for almost all liquid rocket engines during their initial development [1-4]. Transient nozzle side load is therefore considered a high risk item and a critical design issue. For that reason, many research efforts [5-26] have been devoted to understanding the side load physics and their impact on the magnitude of side loads. For regeneratively-cooled engines such as the Space Shuttle Main Engine (SSME), the peak side load generating physics have been identified as the λ shock oscillations across the nozzle lip [7]. For film-cooled engines such as the Japanese LE-7A engine and the U.S. J-2X engine, the major side load generating physics have been associated with the jump of the separation line [3, 8]. Other side load physics such as the Free-Shock Separation (FSS)-to-Restricted-Shock Separation (RSS) transition have been mentioned as the critical physics for the European Vulcain engine [10].

In the aforementioned research efforts, computational fluid dynamics (CFD) have been demonstrated as a powerful analysis and design tool in computing and understanding the underlying transient side load physics. And most of the CFD efforts, have been focused on computing the side load physics with rigid nozzles and not flexible nozzles. However, during actual hot-firing of a rocket engine, the nozzle wall or the structure of the nozzle, flexes or deforms in response to the lateral aerodynamic forces. The deformation of the nozzle wall simultaneously modifies the aerodynamic flowfield and the lateral forces, which in turn affects the nozzle wall deformation. This aeroelastic movement of the nozzle wall, which was not considered in the rigid nozzle modeling, is indeed one of the important side load physics and needs to be considered.

In early 1990's, Pekkari [21] proposed a simplified model to study the aeroelastic stability of the first bending mode of the Vulcain engine. The model consists of an equation of motion describing the displacement of the nozzle wall. For calculation of the aerodynamic load on the wall, a simplified pressure distribution, based on a linearized supersonic flow theory, was used before the separation point. After the separation point, ambient pressure was used. The separation point was established by assuming ratios of separation pressure to ambient pressure as parametric studies. The aerodynamic load calculation of the model was rather crude and the model was later improved by Östlund [10], where the pressure force applied to the nozzle wall, before the separation point, was extracted from three-dimensional Euler simulations, while the separation point was estimated through an empirical criterion. These models, however, did not consider other mode shapes, and the time solutions are quasi-steady and not transient. The quasi-steady solutions could not account for the aerothermodynamic effects of such major side load physics as the combustion wave, shock transitions, λ shock oscillations across the nozzle lip, and jump of the separation line. These two pioneering researches, however, introduced the concept of aeroelastic modeling into nozzle side load studies. In addition, Östlund [10] showed schematically the two asymmetric modes and six buckling and circumferential deformations modes, which were first visualized in nozzle tests of Tuovila and Land [22].

To raise above the simple aeroelastic analysis of Pekkari and Östlund, it seems that two improvements are in order. That is, to refine the crude wall pressure distribution or the Euler solution on the fluid side by the more accurate full CFD solutions, and to upgrade the simple formulation for addressing first bending mode on the structure side with more detailed computational structural dynamics (CSD) formulations that cover all major deformation modes. These improvements have not been realized until 2008, when Zhang, et al [25] embarked on probably the first coupled CFD/CSD methodology for nozzle side load study, by coupling among a full Navier-Stokes solver CFD-FASTRAN, a CSD code FEM-STRESS, and an interface code MDICE, on a quasi-steady, two-dimensional nozzle. In 2013, the same methodology was further demonstrated to show aeroelastic deformation by Zhao et al. [20], on a quasi-steady, three-dimensional analysis of a J-2S nozzle for 0.1818 s of elapsed time. A short while earlier in 2012, Blades, et al. [26] developed a similar methodology to that of Zhao, et al. [20] and Zhang, et al. [25], by coupling a full Navier-Stokes solver CHEM, a CSD code Abaquas, and an interface code CSE, to demonstrate the aeroelastic deformation of a SSME Block II nozzle transient startup for 0.021 s, started at 0.79 s into the start transient. Although these developments represent advances over earlier simple aeroelastic nozzle analyses, it is noted that these analyses ignored chemically reacting flows which plays an important role in all major

side load physics for hot-fired engines. In addition, none of these analyses computed at times or chamber pressures at or close to the occurrence of any major side load events. For example, transient times in the analysis of Blades, et al. ranged from 0.79 s to 0.811 s, which is far from the occurrence of the first major side load physics for SSME start transient – the FSS-to-RSS transition.

Engineers at Marshall Space Flight Center and its contractors have been developing a pressure-based, turbulent, chemically reacting flow CFD methodology for computing the rigid-body transient nozzle side loads. We were the first to inject system modeling for transient SSME nozzle flow computations [24]. We were also the first to capture and anchor major side load physics and its peak magnitudes for regenerative SSME and film cooled nozzles [7, 8]. The anchored CFD methodology has been used to support the design and analysis of the current J-2X engine development and selected efforts were published in literatures [8, 9, 19, 24]. With the recent advances in aeroelastic modeling of nozzle side loads [20, 25, 26], and the recognition of the importance of fluid-structure interaction on nozzle side loads, there is a need to improve our design and analysis methodology by considering the aeroelastic modeling. While examining the recent aeroelastic analyses [20, 25, 26], it occurred to us that the CFD and CSD computations were carried out in different codes and those codes were only connected through an interface code, thus the analyses can only be categorized as loosely coupled aeroelastic simulations [20]. The objective of this effort is therefore to implement the necessary CSD formulations directly into the anchored CFD code, thereby providing stronger coupling of the two-way fluid and structure interactions and potentially be more computationally efficient and accurate. The short term goal of this study is to demonstrate that our implemented algorithms are capable of computing fluid-structure interaction under a multiple-structural-mode environment. As a first attempt, transient analyses of the SSME Block I nozzle startup [7] were performed and the analyses were started at 2.8 s into the transient.

II. Computational Methodology

A. Computational Fluid Dynamics

The computational fluid dynamics (CFD) methodology is based on a multi-dimensional, finite-volume, viscous, chemically reacting, unstructured grid, and pressure-based formulation. Time-varying transport equations of

continuity, species continuity , momentum, total enthalpy, turbulent kinetic energy, and turbulent kinetic energy dissipation were solved using a time-marching sub-iteration scheme and are written as:

$$\frac{\partial \rho}{\partial t} + \frac{\partial}{\partial x_j}\left[\rho\left(u_j - u_{jg}\right)\right] = 0 \tag{1}$$

$$\frac{\partial \rho \alpha_i}{\partial t} + \frac{\partial}{\partial x_j}\left[\rho\left(u_j - u_{jg}\right)\alpha_i\right] = \frac{\partial}{\partial x_j}\left[\left(\rho D + \frac{\mu_t}{\sigma_\alpha}\right)\frac{\partial \alpha_i}{\partial x_j}\right] + \omega_i \tag{2}$$

$$\frac{\partial \rho u_i}{\partial t} + \frac{\partial}{\partial x_j}\left[\rho\left(u_j - u_{jg}\right)u_i\right] = -\frac{\partial p}{\partial x_i} + \frac{\partial \tau_{ij}}{\partial x_j} \tag{3}$$

$$\frac{\partial \rho H}{\partial t} + \frac{\partial}{\partial x_j}\left[\rho\left(u_j - u_{jg}\right)H\right] = \frac{\partial p}{\partial t} + Q_r + \frac{\partial}{\partial x_j}\left(\left(\frac{K}{C_p} + \frac{\mu_t}{\sigma_H}\right)\nabla H\right) + \frac{\partial}{\partial x_j}\left(\left(\left(\mu + \mu_t\right) - \left(\frac{K}{C_p} + \frac{\mu_t}{\sigma_H}\right)\right)\nabla\left(V^2/2\right)\right) \tag{4}$$

$$+ \frac{\partial}{\partial x_j}\left(\left(\frac{K}{C_p} + \frac{\mu_t}{\sigma_H}\right)\left(u_k\frac{\partial u_j}{\partial x_k} - \frac{2}{3}u_j\frac{\partial u_k}{\partial x_k}\right)\right)$$

$$\frac{\partial \rho k}{\partial t} + \frac{\partial}{\partial x_j}\left[\rho\left(u_j - u_{jg}\right)k\right] = \frac{\partial}{\partial x_j}\left[\left(\mu + \frac{\mu_t}{\sigma_k}\right)\frac{\partial k}{\partial x_j}\right] + \rho\left(\Pi - \varepsilon\right) \tag{5}$$

$$\frac{\partial \rho \varepsilon}{\partial t} + \frac{\partial}{\partial x_j}\left[\rho\left(u_j - u_{jg}\right)\varepsilon\right] = \frac{\partial}{\partial x_j}\left[\left(\mu + \frac{\mu_t}{\sigma_\varepsilon}\right)\frac{\partial \varepsilon}{\partial x_j}\right] + \rho\frac{\varepsilon}{k}\left(C_1\Pi - C_2\varepsilon + C_3\Pi^2/\varepsilon\right) \tag{6}$$

A predictor and corrector solution algorithm was employed to provide coupling of the governing equations. A second-order central-difference scheme was employed to discretize the diffusion fluxes and source terms. For the convective terms, a second-order upwind total variation diminishing difference scheme was used. To enhance the temporal accuracy, a second-order backward difference scheme was employed to discretize the temporal terms. Point-implicit method was used to solve the chemical species source terms. Sub-iterations within a time step were used for driving the system of second-order time-accurate equations to convergence. Details of the numerical algorithm can be found in Ref's [27-30].

An extended k-ε turbulence model [31] was used to describe the turbulence. A modified wall function approach was employed to provide wall boundary layer solutions that are less sensitive to the near-wall grid spacing. Consequently, the model has combined the advantages of both the integrated-to-the-wall approach and the conventional law-of-the-wall approach by incorporating a complete velocity profile and a universal temperature profile [32]. A seven-species, nine-reaction detailed mechanism [32] was used to describe the finite-rate, hydrogen/oxygen afterburning combustion kinetics. The seven species are H_2, O_2, H_2O, O, H, OH, and N_2. The thermodynamic properties of the individual species are functions of temperature. The multiphysics pertinent to this study have been anchored in earlier efforts, (e.g., SSME axial force and wall heat transfer [27], SSME startup side

load and dominant shock breathing frequency [7], J-2X startup and shutdown side loads for a nozzlette configuration [8], nozzle film cooling applications [33], and conjugate heat transfer [34], and separated supersonic flows [7, 8, 19, 23, 24]).

The Arbitrary Lagrangian-Eulerian formulation given above in Eqs (1) - (6) is implemented in the flow solver in a manner that fully satisfies the Discrete Geometric Conservation Laws [35] for each cell in the grid; namely, discrete geometric "closure" of the cell at the start and end of each time step, and exact equality between the sum of the discrete volumes swept by all moving faces of the cell with the discrete change in the volume of the cell. Satisfaction of the second Discrete Geometric Conservation Law ensures that spurious sources and fluxes are not generated by the deformation or motion of cells or cell faces, especially those adjacent to moving boundaries. This in turn avoids loss of accuracy in the fluid dynamic computations and in the coupling across the interface between the fluid dynamic and the structural dynamic portions of the problem [20].

B. Computational Structural Dynamics

The structural dynamics response due to fluid flow actions has been analyzed using direct finite-element analysis. The aeroelastic equations of motion of the solid bodies are given by

$$[M]\{\ddot{Y}\}+[C]\{\dot{Y}\}+[K]\{Y\}=\{F\} \tag{7}$$

where $\{Y\}$ is the displacement vector, $[M]$ is the mass matrix, $[C]$ is the damping matrix, $[K]$ is the stiffness matrix, and $\{F\}$ is the force vector due to the aerodynamic loads and shear stresses.

The motion Equation (7) of the structure can be solved using modal approach. On the basis of modal decomposition of the structure motion with the eigenvector of the vibration problem, the displacement, velocity and acceleration can be transformed [25, 35] to the generalized displacement, velocity and acceleration using a transformation matrix, which can be expressed as the following:

$$\{Y\}=[\Phi]\{Z\};\ \{\dot{Y}\}=[\Phi]\{\dot{Z}\};\ \{\ddot{Y}\}=[\Phi]\{\ddot{Z}\} \tag{8}$$

Here [Φ] is the mode shape matrix containing the eigenvectors, orthonormalized with the mass matrix. $\{Z\}, \{\dot{Z}\}, \text{and } \{\ddot{Z}\}$ are the generalized displacement, velocity and acceleration vectors, respectively. The eigenvectors are orthogonal to both mass and stiffness matrixes and if Rayleigh damping is assumed, it is also orthogonal to the damping matrix. Pre-multiplying Equation (8) by $[\Phi]^T$, we get

$$\{\ddot{Z}\}+[\Phi]^T[C][\Phi]\{\dot{Z}\}+[\Phi]^T[K][\Phi]\{Z\}=[\Phi]^T\{F\} \tag{9}$$

where

$$[\Phi]^T[M][\Phi]=1$$

Equation (9) can be written as *n* individual equations, one for each mode, as follows

$$\left.\begin{aligned}&\ddot{z}_i+2\xi_i\omega_i\dot{z}_i+\omega_i^2 z_i=r_i\\&r=\Phi_i^T\{F\}\end{aligned}\right\}\ \text{i}=1,2,...,\text{n} \tag{10}$$

Here ω_i is the natural frequency for the ith mode ξ_i is the corresponding damping parameter for that mode. The solution to Equation (10) can be obtained for each mode using direct integration algorithm. In this effort, since the first several mode shapes are usually important, we chose to compute the first four mode shapes: ovalization, bending, triangle, and square, as shown in Fig. 1. In our current formulation, a structural dynamics software was employed to extract the Eigen modes and Eigen frequencies.

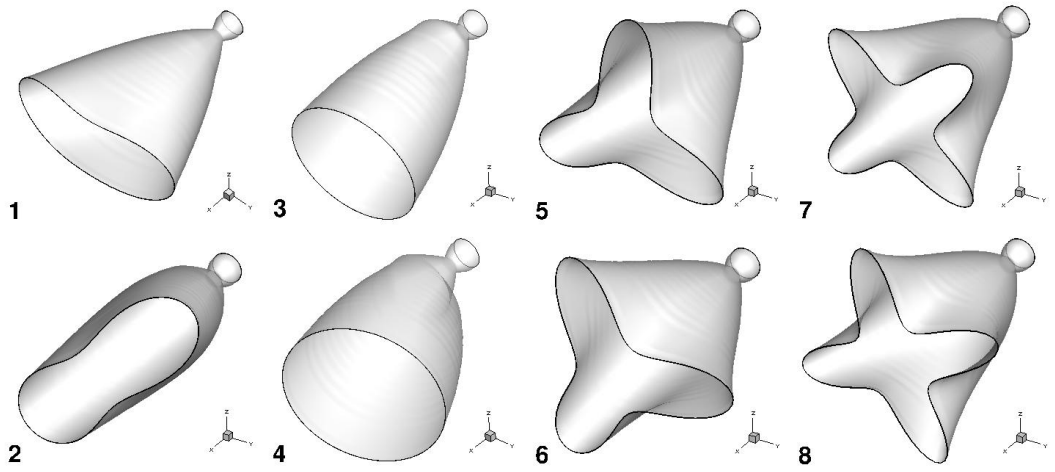

Fig. 1. The four mode shapes.

C. Computational Mesh Dynamics

The geometric and inertial effects of the motions of deforming structures are fed into the flow-field through the varying fluid-dynamic boundary conditions at the surface of structures, which account for the locations and the velocities of these surfaces. In addition, in order to maintain boundary and grid conformity at the fluid-structure interface, the flow-field grid must be deformed to reflect the motion of the fluid-structure interfaces. The new coordinates of the fluid mesh nodes are computed by a computational mesh dynamics. In the present work, the flow-field grid is deformed at every fluid-structure data exchange, which is carried out once at the end of every global time-step, continuously accommodating the deformed shape of the structures in the aeroelastic model. The deformation of the fluid-dynamic grid in this work is accomplished using a spring analog approach, which is applicable for any types of meshes.

The assumption with the spring analog approach is that the mesh nodes are connected like a network of springs. By performing a force balance on each of the "spring elements", an equilibrium balance is sought which provides a smooth mesh. If two elements (nodes) are too close, the spring force will repel the nodes away from each other. Since each nodal position depends on its neighboring nodes, the boundary deformation effects are felt through the mesh domain. Therefore, once the geometries of the

boundary nodes are moved, the distributed spring system settles the nodes into a new equilibrium state which can be modeled by

$$\sum_{j=1}^{N_i} k_{ij}(\delta_i - \delta_j) = 0 \tag{11}$$

for all nodes i in the field. In Eq. (11), δi and δj are the coordinate displacements of node i and its neighboring node j, respectively. N_i is the number of neighboring nodes connected to node i, k_{ij} is the spring stiffness for a given edge i to j is taken to be inversely proportionally to the length of the edge as

$$k_{ij} = \frac{1.}{\sqrt{(x_i - x_j)^2 + (y_i - y_j)^2 + (z_i - z_j)^2}} \tag{12}$$

D. Transient Startup Sequences

Transient system-level simulation is a vital part of the computational methodology, because it provides the time-histories of the inflow properties entering the nozzle. Simply put, the ramp rates, or histories, of the inlet pressure, fluid temperature and species concentrations play an important role in determining the type of side load physics, magnitude and duration of the side loads during the transient operations. In other words, the time-varying inlet flow properties determine the residence times of the side load generating flow physics inside the nozzle.

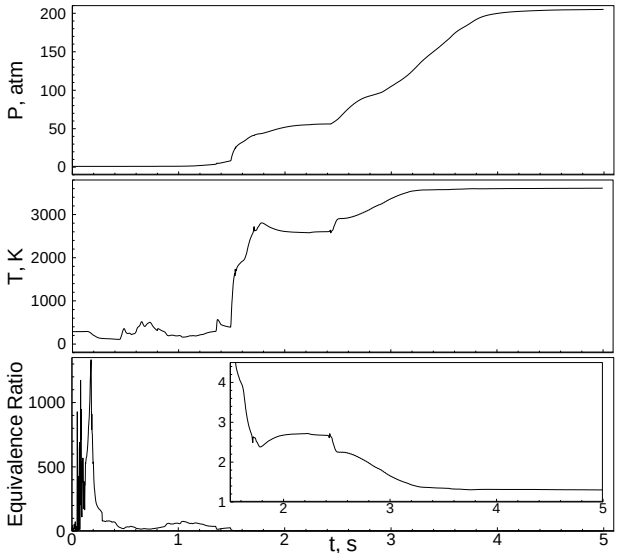

Fig. 2 Computed thruster chamber inlet properties during the start-up transient.

The system-level simulation is based on a lumped, control-volume approach to model the rocket engine as a network of components and sub-components. This

method of transient system-level modeling has been shown to be effective in simulating the low-frequency, transient physics associated with the operation of previous and existing rocket engines (SSME, RL-10, IPD, etc.) and therefore, is an important tool in the design and planning of sequencing the transient events of rocket engine operation. Figure 2 shows the major inlet flow properties obtained from the system model: the time-varying inlet pressure, temperature, and equivalence ratio profiles. These time-varying inlet properties were used at the injector faceplate of the thrust chamber for the CFD computation. Two significant pressure rise events can be identified in the inlet pressure history of Fig. 2. The first one occurs at 1.5 s due to oxygen prime, while the second one occurs at about 2.4 s, caused by the step opening of the oxygen valves in the pre-burners. The inlet temperature history shows a sharp jump at 1.5 s, leveling off after 1.75 s, jumps a little bit again at 2.4s, and increases linearly until around 3.1 s when it reaches the final temperature. The inlet equivalence ratio history shows that the thruster environment is fuel rich throughout the start-up transient, especially in the first 1.5 s, setting up the potential for afterburning. That turns out to be the source of the combustion wave, because the pressure jump at 1.5 s increases the reaction rate of afterburning, which leads to the generation of the combustion wave. Afterburning plays an important part in the subsequent asymmetric flow physics such as the shock transitions and shock breathings across the nozzle lip. As mentioned in the beginning of this section, that the route or history between the starting and end points of any of the curves in Fig. 2 influences the side load physics intimately, any simplification on any part of the sequence may run the risk of missing or degradation of important side load physics. This SSME start transient process involves thermal-fluid physics phenomena and safety-based operating practices that are typical of a conventional liquid hydrogen/liquid oxygen rocket engine.

III. Computational Grid Generation

A grid study procedure was developed for transient nozzle side load computations following the results of a SSME transient nozzle side load study [7], by assuming the grid study can be performed on steady-state axial force computations. The steady-state axial force study was performed in a separate effort [27] in which axial forces were calculated for two axisymmetric grids and two three-dimensional grids. The results for the two three-dimensional grids are shown in Table 1. This procedure is necessitated by the cost-prohibitive computational requirement for computing a three-dimensional, transient, turbulent reacting flow for 3 to 5 s, especially for sea level simulations since both the flow residence time and chemical reaction time are long. In addition, since the peak side force is

usually a small percentage of the axial force, it is further assumed that if the grid density is suitable for the steady-state axial force calculations, then it is likely adequate for the transient side force analyses. This procedure was demonstrated adequate as described in the SSME side load study [7]. The predicted peak side loads and dominant frequency for sea level startup transient agreed very well with those of tests [7].

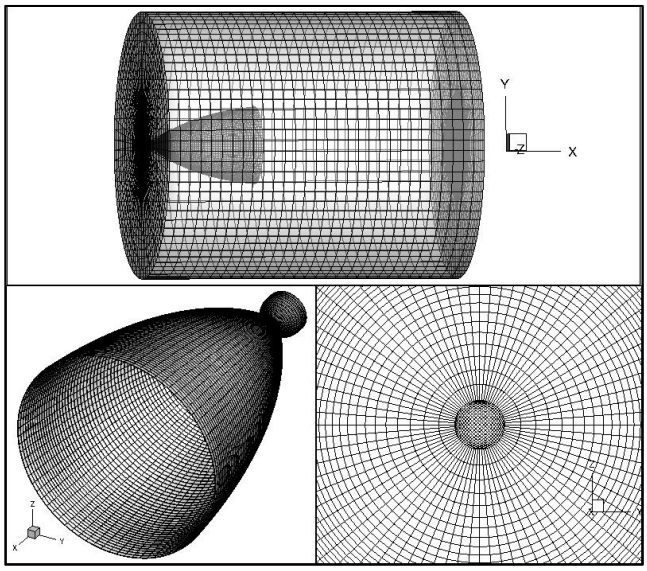

Fig. 3 Computational grid layout for Case 3d11.

In Case 3d6 [7], the grid was generated by rotating an axisymmetric grid and a circumferential divisional number of 72 was used. Structured cells were used in the thruster and plume region, and unstructured cells were used in the ambient region. In Case 3d9 [9], Unstructured cells were used all over the computational domain, except for the wall boundary layers. Structure cells are therefore predominant in Case 3d6, while unstructured cells are of the majority in Case 3d9. This can be seen from Table 1 where Case 3d6 has more grid points and Case 3d9 has more number of cells. As pointed out in Table 1, the predicted specific impulse (ISP) from Case 3d6 agreed better with the target than that of Case 3d9, that is because the structured cells are of better quality than that of the unstructured cells [7]. In this effort (Case 3d11), the grid generation strategy follows that of Case 3d6, with structured cells in the thruster and plume region and unstructured cells in the ambient region. In addition, with the additional work load coming from solving structural dynamics equation and for a first attempt, the total number of points and cells are reduced by carefully allocating grid points, yet maintaining reasonable axial force result, as shown in Table 1. Figure 3 shows the grid layout for case 3d11. The top layout shows the thruster is embedded in the freestream boundary and the bottom-left plot shows the layout of the thruster. Note the centerline is replaced by a "circular rod" of structured cells, which removes the degenerated hexagonal cells surrounding the centerline as a result of rotating around the centerline, as shown in the bottom-right plot. The circumferential division number is increased slightly to 84 from the 72 of case 3d6.

Table 1. A comparison of computational grids.

Case	No. points	No. cells	ISP	Ref.
3d6	1,286,934	1,275,120	453.27	22
3d9	418,165	1,732,081	450.00	22
3d11	576,880	529,487	453.61	this work
Target			453.30	

IV. Boundary and Inlet Conditions

Since SSME is a first stage engine, fixed freestream boundary conditions were set corresponding to sea level. No-slip condition was specified for the solid walls. Time-varying inlet flow boundary conditions were used at the main combustion chamber (MCC) inlet. These inlet flow properties obtained from the engine system simulation include the time varying total pressure, temperature and propellant compositions. The time varying propellant composition was preprocessed with the Chemical Equilibrium Calculation program [36], assuming the propellants were ignited to reach equilibrium composition immediately beyond the injector faceplate. The larger than unity equivalence ratio throughout the 5 s ramp period indicates the SSME is operated at fuel rich condition and the inlet composition contains mostly steam and excess hydrogen, as shown in Fig. 2. At the start command, or time zero, the entire flowfield was initialized with quiescent air. The presence of air allows the afterburning with the excess fuel which contributes to the side force physics. Since our goal is to demonstrate the aeroelastic modeling algorithm and as a first attempt, the transient

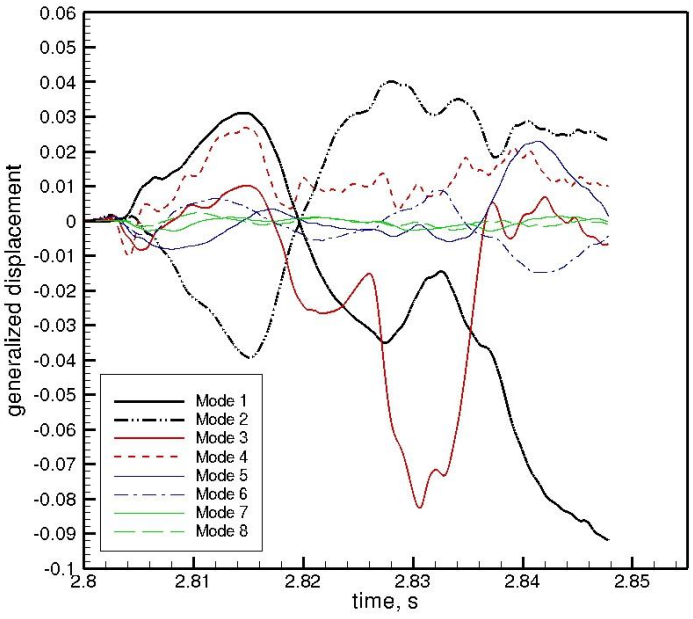

Fig. 4 Computed generalized displacement histories.

aeroelastic computation started from a rigid nozzle solution at 2.8 s.

V. Results and Discussion

For these transient aeroelastic computations at sea level, the reaction rates of combustion are high and global time steps ranging from 1 to 10 μs are expected to be used throughout the computations. These global time steps used correspond to Courant-Friedrichs-Lewy numbers ranging approximately from 0.1 to unity.

Figure 4 shows the computed time-varying generalized displacements contributed from the eight mode shapes considered in this study. As indicated in Fig. 1, modes 1 and 2 are associated with the ovalization, modes 3 and 4 are associated with the first bending, modes 5 and 6 are associated with the triangle, and modes 7 and 8 are associated with the square. It can be seen from Fig. 4 that modes 1 and 2 (or the ovalization mode), and modes 3 and 4 (or the first bending mode) dominates the generalized displacement, as observed from the hot-fire tests, while modes 5 and 6 have a much smaller contribution and modes 7 and 8 have negligible influences. This is consistent with the observation [36] that for most of the engineering structures, the number of significant modes by which almost 95% of the mass has participated is usually about three to twenty-five. For nozzle structures, Östland [10] observed that the two lowest asymmetric modes may generate side loads. Östland [10] also noted that when the bending mode is excited in weak nozzle structures, aeroelastic effects can no longer be ignored.

A close look at Fig. 4 reveals that the first increase in generalized displacement occurred at 2.815 s, at that time mode 1 reached a value of -0.04, followed by 0.03 of mode 1 and -0.026 of mode 4. At 2.829 s, modes 1 and 2 reached generalized displacements of about -0.034 and 0.03, but mode 3 dominates and reached a value of -0.064. At 2.831 s, mode 3 still dominates and reached a

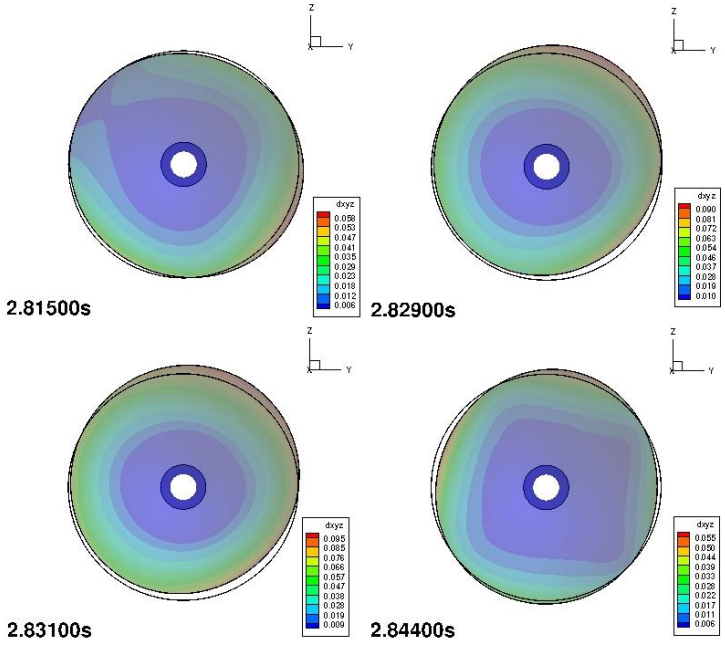

Fig. 5 End views of computed nozzle shapes and deformation contours.

local peak generalized displacement of -0.084, while modes 1 and 2 maintained generalized displacements at about -0.02 and 0.036, respectively. After which mode 3 fades, but mode 1 gains ground. At 2.844 s into the start transient, mode 1 reached a generalized displacement of 0.086, mode 2 arrived at about 0.025, while modes 5 and 6 reached generalized displacements of 0.014 and -0.014, respectively. The generalized displacement plot shows which mode shape dominates at different transient startup times.

Figure 5 shows the nozzle end views of the state of nozzle deformation and the deformation contours at the aforementioned four time slices. The deformation contours are represented by calculated total physical displacements. The exit plane of the rigid nozzle is shown as a reference. At 2.815 s, slight ovalization coming from both modes 1 and 2 are displayed. At 2.829 s, the effect of mode 3 dominates and its effect peaks at 2.831 s. At 2.844 s, mode 1 regains dominance and a slight ovalization is shown. Figure 6 shows the nozzle side views of the nozzle shapes and deformation contours at the same four time slices. The effect of first bending can be seen at plots of 2.829 s and 2.831 s, while the effect of a slight ovalization can be seen at 2.815 s and the effect of a slightly stronger ovalization at be seen at 2.844 s.

Nozzle wall deformation affects the advancing Mach disk flow, which in turn influences the interior pressures. Figure 7 shows a comparison of the computed axial wall pressure profiles for the rigid nozzle and flexible nozzle along the dividing lines of the four quadrants. These axial pressure profiles are taken at 2.846 s when mode 1 dominates. At this time slice, the profiles of the rigid nozzle appear to be enclosed by those of the flexible nozzle. That is, the pressure profiles of the flexible nozzle are either above or below those of the rigid nozzle, showing the effect of nozzle wall deformation. The pressure profiles of the flexible nozzle show some waviness, while those of the rigid nozzle are smooth. The profiles of the rigid nozzle and flexible nozzle start to separate from each other deep

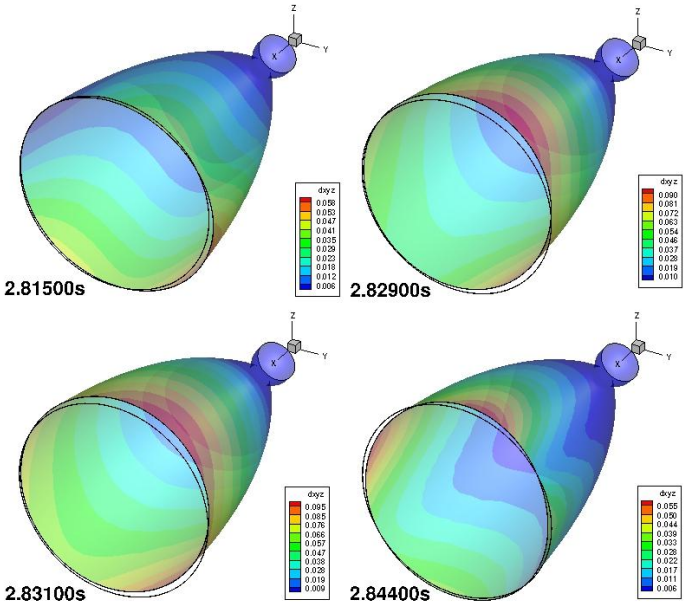

Fig. 6 Side views of computed nozzle shape and deformation contours.

into the nozzle, or about 0.6 m away from the throat. The rise of the wall pressures to near 1 atm near the end of the nozzle showing the typical "end effect" physics described by Nave and Coffey [1].

Figure 8 shows the computed lateral physical displacement histories for four monitor points. These four monitor points are located at 0, 90, 180 and 270 degrees circumferentially, and located just off the nozzle exit plane axially. It can be seen that all four monitor points experience different displacement histories, indicating the deformation is mostly asymmetric. It can also be seen that the physical displacement histories displayed in Fig. 8 correspond well with the generalized displacement histories shown in Fig. 4, in terms of the timings of the peaks and valleys. That is, The local peaks in physical displacement agree with those in generalized displacement. It is noted that the computed physical lateral displacements shown in Fig. 8 represent the contribution from all the structural modes considered, while the computed generalized displacements shown in Fig. 4 depicts the contributions from each and every mode shapes. These two figures therefore complement each other. It can be inferred the largest physical displacement shown in Fig. 8 comes from the impact of the first bending mode.

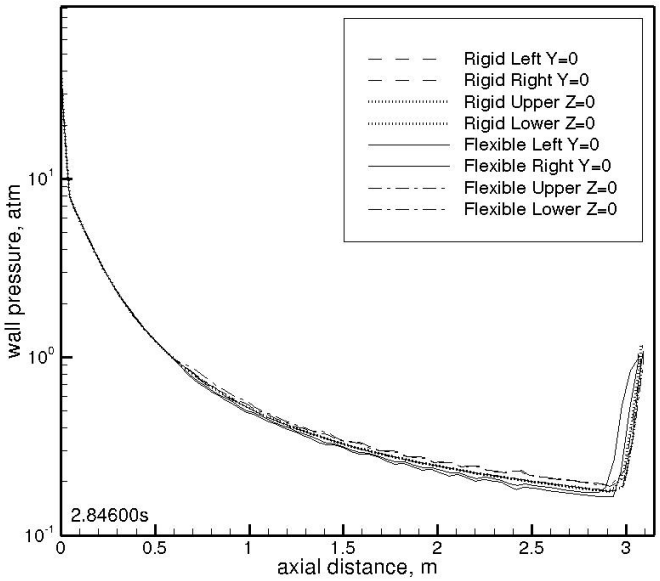

Fig. 7 Comparison of axial nozzle wall pressure profiles.

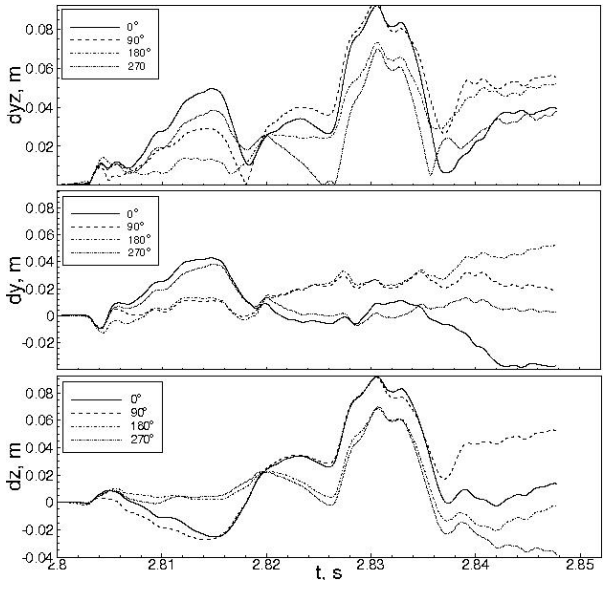

Fig. 8 computed physical lateral displacement histories at four monitor points.

Figure 9 shows the computed side load histories from both the rigid and flexible nozzles. It can be seen that the two side load histories show different

characteristics and the effect of deformation is demonstrated. Although the peak side load for the flexible is about 56 kN, which is only slightly above that of the rigid nozzle at about 50 kN. This is because although the Mach disks have been oscillated inside the nozzle, they have not been oscillated across the nozzle lip yet, due to the limited elapsed times experienced.

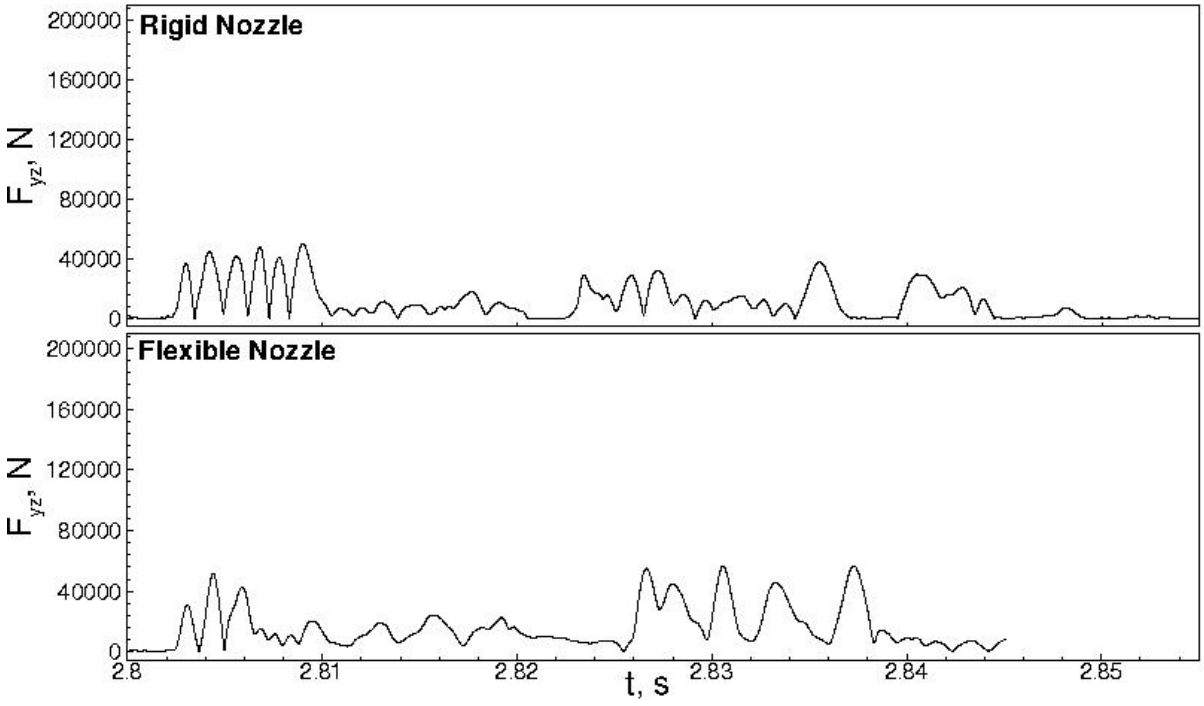

Fig. 9 Computed side load histories.

VI. Conclusion

An aeroelastic modeling capability is being developed for transient nozzle side load analysis. The objective is to implement the necessary CSD formulations directly into the anchored CFD code, thereby providing stronger coupling of the two-way fluid and structure interactions and potentially be more computationally efficient and accurate. As a first attempt, three-dimensional simulations of the transient startup sequence of the SSME Block I nozzle has been performed, to demonstrate that our implemented algorithms are capable of computing fluid-structure interaction under a multiple-structural-mode environment. The computed generalized displacements, deformed nozzle shapes and deformations contours, physical lateral displacements, axial nozzle wall pressure

profiles and side loads, demonstrated our implemented algorithms are working properly. The dominating mode shapes computed are the first two mode shapes: ovalization and first bending, agreeing with the observations.

Acknowledgments

The first author was partially supported by the J-2X engine program at NASA Marshall Space Flight Center, in which Mike Shadoan managed the nozzle project and Marcus Neely managed the system test project. Professor Zhao was partially supported by a Seed Grant from National Science Foundation and by a NASA 2012 Summer Faculty Fellowship. The authors acknowledge James Beck of Pratt-Whitney Rocketdyne for his insight in fluid-structure interactions. The authors also wish to thank Eric Blades of ATA Engineering for several initial discussions.

References

[1] Nave, L.H., and Coffey, G.A., "Sea Level Side Loads in High-Area-Ratio Rocket Engines," AIAA Paper 73-1284, Nov. 1973.

[2] Cikanek, H.A., "Characteristics of Space Shuttle Main Engine Failures," AIAA Paper 87-1939, June 1987.

[3] Watanabe, Y., Sakazume, N., and Tsuboi, M., "LE-7A Engine Nozzle Problems During the Transient Operations," AIAA Paper 2002-3841, July 2002.

[4] Shi, J., "Rocket Engine Nozzle Side Load Transient Analysis methodology – A Practical Approach," AIAA Paper 2005 – 1860, April 2005.

[5] Hagemann, G., Terhardt, M., Frey, M., Reijasse, P., Onofri, M., Nasuti, F., and Ostlund, J., "Flow Separation and Side-Loads in Rocket Nozzles," 4th International Symposium on Liquid Space Propulsion, March 12-15, 2000, DLR Lampoldshausen, pp. 1-19.

[6] Yonezawa, K., Yokota, K., Tsujimoto, K., Sakazume, N., and Watanabe, Y., "Three-Dimensional Unsteady Flow Simulation of Compressed Truncated Perfect nozzles," AIAA Paper 2002-3991, July 2002.

[7] Wang, T.-S., "Transient Three-Dimensional Startup Side Load Analysis of a Regeneratively Cooled Nozzle," *Shock Waves – An International Journal on Shock Waves, Detonations and Explosions.* Vol. 19, Issue 3, 2009, pp. 251~264. DOI: 10.1007/s00193-009-0201-2.

[8] Wang, T.-S., and Guidos, M., "Transient Three-Dimensional Side Load Analysis of a Film-Cooled Nozzle," *Journal of Propulsion and Power*, Vol. 25, No. 6, 2009, pp. 1272-1280, doi: 10.2514/1.41025.

[9] Wang, T.-S., Lin, J., Ruf, J., Guidos, M., and Cheng, G.C., "Effect of Coolant Flow Distribution on Transient Side Load of Film Cooled Nozzles," *Journal of Propulsion and Power,* Vol. 28, No. 5, September-October, 2012, pp. 1081-1090. doi:10.2514/1.B34397

[10] Östland, J., "Supersonic Flow Separation with Application to Rocket Engine Nozzles," Doctoral Thesis, Royal Institute of Technology, Stockholm, Department of Mechanics, Sweden, 2004.

[11] Deck, S., "Delayed Detached Eddy Simulation of the End-Effect Regime and Side-Loads in an Overexpanded Nozzle Flow," *Shock Waves – An International Journal on Shock Waves, Detonations and Explosions.* Vol. 19, Issue 3, 2009, pp. 239~249. DOI: 10.1007/s00193-009-0199-5.

[12] Hadjada, A., and Onofri, M., "Nozzle Flow Separation," *Shock Waves – An International Journal on Shock Waves, Detonations and Explosions.* Vol. 19, Issue 3, 2009, pp. 163~169. DOI: 10.1007/s00193-009-0209-7.

[13] Tomita, T., Takahashi, M., Sasaki, M., Sakamoto, H., Takahashi, M., Tamura, H., "Experimental Evaluation of Side Loads in LE-7A Prototype Engine Nozzle," *Shock Waves – An International Journal on Shock Waves, Detonations and Explosions.* Vol. 19, Issue 3, 2009, pp. 213~228. DOI: 10.1007/s00193-009-0191-0.

[14] Nguyen, A.T., Deniau, H., Girard, S., and De Roquefort, T.A., "Unsteadiness of Flow Separation and End-Effects Regime in a Thrust-Optimized Contour Rocket Nozzle," Flow, Turbulence and Combustion, Vol. 71, No. 1-4, 2003, pp.161-181.

[15] Deck S., and Guillen, P., "Numerical Simulation of Side loads in an Ideal Truncated Nozzle," *Journal of Propulsion and Power*, Vol. 18, No. 2, 2002, pp. 261-269. doi: 10.2514/2.5965

[16] Shimizu, T., Miyajima, H., and Kodera, M., "Numerical Study of Restricted Shock Separation on a Compressed Truncated Perfect Nozzle," *AIAA Journal*, Vol. 44, No. 3, 2006, pp. 576-584.

[17] Stark, R., and Genin, C., "Optimisation of a Rocker Nozzle Side Load Reduction Device," AIAA Paper 2012-3970, July 2012.

[18] Reijasse, Ph., and Boccaletto, L., "Influence of Film Cooling on Nozzle Side loads," AIAA Paper 2008-392, Jan. 2008.

[19] Wang, T.-S., Lin, J., Ruf, J., and Guidos, M., "Transient Three-Dimensional Side Load Analysis of Out-of-Round Film Cooled Nozzles," *Journal of Propulsion and Power,* Vol. 27, No. 4, July-August, 2011, pp. 899-907, doi: 10.2514/1.B34082.

[20] Zhao, X., Bayyuk, S,m and Zhang, S.J., "Aeroelastic Response of Rocket Nozzles to Asymmetric Thrust Loading", Computer and Fluids, Vol. 76, 2013, pp. 128-148.

[21] Pekkari, L.-O., "Aeroelastic Analysis of Side Load in Supersonic Nozzles with Separated Flow." AIAA Paper 1994-3377, June 1994.

[22] Tuovila, W.J., and Land, N.S., "Experimental Study of Aeroelastic Instability of Overexpanded Rocket Nozzle Extensions," NASA TN D-4471, 1968.

[23] Wang, T.-S., Lin, J., and Guidos, M., "Transient Side-Load Analysis of Out-of-Round Film-Cooled Nozzle Extensions," AIAA Paper 2012-3968, July 2012.

[24] Wang, T.-S., "Numerical Study of the Transient Nozzle Flow Separation of Liquid Rocket Engines," *Computational Fluid Dynamics Journal*, Vol.1, No.3, Oct. 1992, pp. 319-328.

[25] Zhang, S.J., Fuchiwaki, T., and Xiang, Zhao, "Aeroelastic Coupling and Side Load in Rocket Nozzles," AIAA Paper 2008-4064, 2008.

[26] Blades, E.L., Luke, E.A., and Ruf, J., "Fully Coupled Fluid-Structure Interaction Simulations of Rocket Engine Side Loads," AIAA Paper 2012-3969, July 2012.

[27] Wang, T.-S., "Multidimensional Unstructured-Grid Liquid Rocket Engine Nozzle Performance and Heat Transfer Analysis," *Journal of Propulsion and Power,* Vol. 22, No. 1, January-February, 2006, pp. 78-84.

[28] Shang, H.M., and Chen, Y.-S., "Unstructured Adaptive Grid method for Reacting Flow Computation," AIAA Paper 1997-3183, July 1997.

[29] Wang, T.-S., Chen, Y.-S., Liu, J., Myrabo, L.N., and Mead, F.B. Jr., "Advanced Performance Modeling of Experimental Laser Lightcraft," *Journal of Propulsion and Power,* Vol. 18, No. 6, 2002, pp. 1129-1138.

[30] Chang, G., Ito, Y., Ross, D., Chen. Y.-S., Zhang S., and Wang, T.-S., "Numerical Simulations of Single Flow Element in a Nuclear Thermal Thrust Chamber" AIAA Paper 2007-4143, June 2007.

[31] Chen, Y.-S., and Kim, S. W., "Computation of Turbulent Flows Using an Extended k-ε Turbulence Closure Model," NASA CR-179204, Oct. 1987.

[32] Wang, T.-S., Droege, A., D'Agostino, M., Lee, Y.-C., and Williams, R., "Asymmetric Base-Bleed Effect on X-33 Aerospike Plume Induced Base-Heating Environment," *Journal of Propulsion and Power,* Vol. 20, No. 3, 2004, pp. 385-393.

[33] Chen, Y.-S., Cheng, G.C., and Farmer, R.C., "Reacting and Non-Reacting Flow Simulation for Film Cooling in 2-D Supersonic Flows," AIAA Paper 92-3602, July 1992.

[34] Wang, T.-S., Canabal, F., Chen, Y.-S., and Cheng, G.C., "Multiphysics Computational Analysis of a Solid-Core Nuclear Thermal Engine Thrust Chamber," *Journal of Propulsion and Power,* Vol. 26, No. 3, May-June, 2010, pp. 407-414.

[35] Thomas, P. and Lombard, C., "Geometric Conservation Law and its Application to Flow Computations on Moving Grids," *AIAA Journal, AIAA,* Vol. 17, No. 10, 1979, pp. 1030-1037.

[36] Giosan, Ioan. "Dynamic Analysis with Damping for Free Standing Structures using Mechanical Event Simulation." University" Politehnica" of Bucharest Scientific Bulletin, Series C: Electrical Engineering 68.3 (2006): 15-30.

[37] Svehla, R.A., McBride, B.J., "FORTRAN IV Computer Program for Calculation of Thermodynamic and Transport Properties of Complex Chemical Systems," NASA TN D-7056, (1973)